

## Article

# CerAMufacturing of Aluminum Nitride with High Thermal Conductivity via Lithography-Based Ceramic Vat Photopolymerization (CerAM VPP)

Eric Schwarzer-Fischer \*, Uwe Scheithauer  and Alexander MichaelisFraunhofer Institut für Keramische Technologien und Systeme (IKTS), Winterbergstraße 28,  
01277 Dresden, Germany

\* Correspondence: eric.schwarzer-fischer@ikts.fraunhofer.de; Tel.: +49-351-2553-7625

**Abstract:** Aluminum nitride (AlN) is an excellent material for heat sinks and is used, for example, in high-performance electronics, high-power LEDs and photovoltaics. In order to meet the constantly increasing demands on substrate materials and heat sinks resulting from the permanent increase in power density and resulting heat in electronic components, new types of components made of high-performance materials with highly complex geometries are required. In this work, AlN based on a commercial powder (“TOYALNITE®”-JCGA-BLY5 by Toyal Europe), was successfully qualified for an AM technology through suspension and process development for CerAM VPP—a DLP-based vat photo polymerization technology. The properties of the components were characterized along the entire process chain, achieving densities of 3.33 g/cm<sup>3</sup> (>99% Th.D.) and excellent thermal conductivities of more than 180 W/mK, which are comparable to state-of-the-art for conventionally manufactured AlN components. Homogeneous microstructures of good quality confirm the measured density and thermal conductivity. A complex-shaped component usable for an exemplary heating–cooling application demonstrates the potential of this development.

**Keywords:** aluminum nitride (AlN); additive manufacturing (AM); CerAMufacturing; vat photopolymerization (VPP); digital light processing (DLP); lithography-based ceramic manufacturing (LCM); thermal conductivity



**Citation:** Schwarzer-Fischer, E.; Scheithauer, U.; Michaelis, A. CerAMufacturing of Aluminum Nitride with High Thermal Conductivity via Lithography-Based Ceramic Vat Photopolymerization (CerAM VPP). *Ceramics* **2023**, *6*, 416–431. <https://doi.org/10.3390/ceramics6010024>

Academic Editor: Gilbert Fantozzi

Received: 21 December 2022

Revised: 13 January 2023

Accepted: 31 January 2023

Published: 2 February 2023



**Copyright:** © 2023 by the authors. Licensee MDPI, Basel, Switzerland. This article is an open access article distributed under the terms and conditions of the Creative Commons Attribution (CC BY) license (<https://creativecommons.org/licenses/by/4.0/>).

## 1. Introduction

Aluminum nitride (AlN) is a material with a unique combination of properties. A very high thermal conductivity, which, with values of 150 W/m·K to more than 250 W/(m·K), is in the range of the thermal conductivity of magnesium, silicon, or aluminum, is paired with a very low electrical conductivity (1013 Ohm·mm [1]). Therefore, AlN is an excellent material for heat sinks, and it is used, for example, in the fields of high-performance electronics, high-performance LEDs, photovoltaic systems [2] and many other technical areas [3,4]. In addition, direct metallization of the AlN surface is possible, allowing direct interfacing of electronic components, e.g., by “chip-on-heatsink” technology [5]. This not only enables miniaturization of the overall system, but also a significant reduction in the effort and risk of defects during assembly compared to conventionally assembled power modules [5]. Various implementation examples for different applications are available at [6].

Commercially available, high-quality AlN ceramics have a thermal conductivity of approximately 170–180 W/(m·K) at room temperature [7–9]. Important factors that negatively influence this property are foreign atoms and the associated vacancies in the crystal lattice, pores, cracks, grain boundaries, and secondary phases, and the incorporation of oxygen into the AlN lattice, which is considered the main impurity in the microstructure [10–12].

Usually, AlN ceramics are produced using pressure-less sintering at temperatures of about 1800 °C in a nitrogen atmosphere and suitable sintering additives such as yttria to

achieve sufficient densification and high thermal conductivity [13]. In this context, many studies shed light on the influence and control of the sintering atmosphere on the properties of AlN [14–16]. A reduction of the lattice oxygen can be achieved through long dwell times at high sintering temperatures ( $>1800$  °C) using a graphite furnace [17–19]. However, caution is required here, as this is accompanied by grain growth of AlN and a reduction in strength [20].

The power density, and thus also the heat produced in electronic components, which must be dissipated quickly, is constantly increasing due to raising requirements. This also results in permanently increasing demands on the substrate materials and heat sinks.

The shaping of AlN is mainly achieved through conventional methods such as uniaxial or cold isostatic dry pressing [21] and solvent-based tape casting [22–24], but this only allows the manufacturing of substrates with limited geometrical complexity [7–9,25].

Modern shaping methods from the class of additive manufacturing (AM) technologies, which has become a particular focus in the field of ceramics in recent years, expand the degrees of freedom in design and thus offer the possibility of realizing ceramic materials of higher complexity for a wide range of applications [26,27]. Many AM technologies have already been qualified for different ceramics. Processes such as robo-casting [28] or binder jetting [29,30] have already successfully shaped AlN, but with limitations in component quality such as density, surface quality or resolution.

In terms of resolution and component quality, AM technologies from the vat photo polymerization (VPP) group are currently unrivalled in the field of ceramics and offer the possibility of realizing dense components of high complexity [31–33]. In stereolithography (SLA), which is a typical representative of this technology group, a component is built up layer by layer through polymerization of a photoreactive suspension caused by spatially resolved irradiation using a laser. A further development of this is digital light processing (DLP) technology, in which light beams are directed as a layered image via a projector onto the surface of a photoreactive ceramic suspension, thus simultaneously solidifying all selected areas of the layer of a disassembled component and thereby creating the component. Using suspensions, which are highly filled with ceramic particles, a ceramic green body can be additively manufactured in the same way (“CerAMfacturing”), which is subsequently further processed according to the usual ceramic process chain via debinding and sintering, in order to obtain ceramic components with approximately the same properties as conventionally manufactured components [31–33]. Ceramics processed so far are  $\text{Al}_2\text{O}_3$ ,  $\text{ZrO}_2$ , ATZ, ZTA or HAp. Attempts to process darker (light absorbing) materials such as  $\text{Si}_3\text{N}_4$  [34,35] or SiC [36] have also been carried out but are still under development.

Recently, Rauchenecker et al. successfully investigated the production of AlN via DLP and obtained good results (thermal conductivities of  $160 \text{ W}/(\text{m}\cdot\text{K})$ ) via sintering at a temperature of  $1700$  °C [37] and compared their results with previous publications in this field [38–40].

Since the demand for complex-shaped AlN with good properties is high and only a few materials are available, the focus in this study is to qualify a commercial AlN powder for the DLP-based CerAM VPP process (Lithoz LCM technology) using suspension development to allow for the manufacturing of complex components with high thermal conductivity after sintering.

## 2. Materials and Methods

### 2.1. Raw Materials

The used ceramic raw material of this study is a “yellowish-white” AlN powder distributed by KRAHN Chemie Deutschland, which is offered under the name “TOYALNITE®-JCGA-BLY5” by Toyal Europe. Added with approx. 5 wt% yttria as sintering additive, it is considered as “ready to sinter”.

According to the data for powder pressing, a sinter density of at least approx.  $3.32 \text{ g}/\text{cm}^3$  ( $\rho_{\text{rel.D.}} = 99.1\%$ ) at a sintering temperature of  $1850$  °C (7 h dwell time), as well as a thermal conductivity of  $>170 \text{ W}/(\text{m}\cdot\text{K})$ , is achievable. These values are used as a reference.

Before starting suspension development, the particle size distribution (PSD) as well as the specific BET surface of the AlN powder were estimated via laser diffraction (Mastersizer 2000; Malvern Panalytical Ltd., Malvern, UK) and gas absorption for BET measurement (ASAP2020; Micromeritics GmbH, Unterschleißheim, Germany).

In general, VPP technologies require a photoreactive system consisting of various monomers with different functionalities and a photoinitiator (PI). The formulation of such a system is tailored with respect to the required properties, for example, flexibility or strength of the green body.

In a previous study [35], a system for nitrides, especially silicon nitride, suitable for processing with the DLP used here, has already been successfully developed. Based on the results, a low viscous tetrafunctional polyether acrylate (PPTTA from BASF, Ludwigshafen, Germany) and an aliphatic urethane di-acrylate (UA, BASF, Germany) were chosen as photosensitive resin monomers in a weight ratio of 7:3. Omnirad 784 (o784; I1), as a representative for Norrish Type I (IGM Resins, Waalwijk, The Netherlands), and camphorquinone (CQ; I2) in combination with an ethylamine (I2) activator, as a representative for Norrish Type II, were used in combination as a photoinitiation system to initiate polymerization of the acrylates after exposure to the light source of the printing device (wavelength  $\lambda = 451$  nm). Achieving a good dispersion of the AlN-powder, a solvent-free phosphoric ester salt of a high molecular weight copolymer with pigment-affine groups, which is particularly suitable for non-polar systems (BYK-Chemie GmbH, Wesel, Germany), has been used as a first dispersant (FD). As an alternative for optimizing the flow behavior, a 100% active polymeric dispersant (AD) from Lubrizol was used. Furthermore, polypropylene glycol (PPG, Sigma-Aldrich, St. Louis, MI, USA) was added as plasticizing fluid to reduce the viscosity and the risk of defects due to thermal debinding [41].

## 2.2. Preparation of AlN Suspensions

Based on the raw materials, photoreactive ceramic suspension formulations with various AlN contents were developed and prepared. The photosensitive resin was prepared at first using a planetary centrifugal mixer (thinky ARV 10, C3-Prozess und Analysentechnik GmbH, Haar, Germany) for the homogenization (8 min at 2000 rpm) of the PPTTA, the UA and the photoinitiator as well as the fluid PPG. In addition, an ultrasonic bath was used to dissolve residual initiator agglomerates followed by a second mixing step (8 min at 2000 rpm) in the thinky mixer. Finally, the dispersant and the AlN powder were added to the prepared resin and treated two times for 8 min at 2000 rpm in the thinky mixer to achieve a good deagglomeration as well as a stable suspension. As an intermediate step, the suspension was dissolved in an ultrasonic bath for 5 min, followed by a second mixing step for homogenization (thinky mixer).

The suspension development happened in four stages (Table 1). First (I), the solid content was investigated to achieve a high solid loading. Therefore, the AlN content was varied between 10 and 44 vol% (labeled f1–f7; I1-o784 with 0.016 mol/L and I2-CQ with 0.038 mol/L) by a constant dispersant content (FD) of 1.3 wt% (related to the AlN content). Afterwards (II), the AlN content was increased up to 44, 46 and 48 vol% (labeled f8–f10) and the dispersant content (FD) to 1.5 wt%. Still reducing the viscosity at low shear rates, an alternative dispersant (AD) was investigated in a third step (III) for itself (f11) and in combination with the FD (suspensions f12–f14), at a constant AlN content of 48 vol%.

In the fourth stage (IV), the initiator content was adjusted in suspensions f8–f10 (I1-o784 with 0.009 mol/L and I2-CQ with 0.032 mol/L) to achieve a better photosensitivity, leading to adequate photo polymerization properties (sufficient cure depth) and layer formation quality (low over-exposure effects).

**Table 1.** Nomenclature of suspension formulations and investigation steps.

Stage	Formulation	Solid Content [vol%]	Dispersant [wt%]	PI-Type	PI-Concentration [mol/L]
I	f1	10			
	f2	15			
	f3	20			
	f4	25	FD 1.3	o784	c = 0.016
	f5	33		CQ	c = 0.038
	f6	39			
	f7	44			
II + IV *	f8	44		o784	* c = 0.009
	f9	46	FD 1.5	CQ	* c = 0.032
	f10	58			
III	f11		AD 1.5		
	f12		FD 1.0 + AD 0.5	o784	c = 0.016
	f13	48	FD 0.5 + AD 1.0	CQ	c = 0.038
	f14		FD 1.0 + AD 1.0		

\* Formulations f8–f10 also include stage 4 development with adjusted PI concentration.

### 2.3. Characterization of AlN Suspensions

The rheological properties were characterized by measuring the shear viscosity (Modular Compact Rheometer MCR302 with a cone/plate measurement system, Anton Paar, Graz, Austria) dependent upon the powder and dispersant content. Viscoelastic behavior (decreasing dynamic viscosity with increasing shear rates) in a low viscosity range (20 to 80 Pa·s at shear rates of 1–100 s<sup>−1</sup>/s) should be a present characteristic for use with CerAM VPP, due to the rotational suspension-coating mechanism of the process. The flow behavior, especially the dynamic viscosity, was measured at shear rates in a range of 0.1 to 1000 1/s.

The curing properties, i.e., the light-induced polymerization of one layer, were determined by measuring the curing depth of a polymerized specimen (approx. 1 mL) after exposure dependent upon the suspension's formulation, especially the solid and initiator content as well as the used energy dose (451 nm wavelength), a value resulting from the irradiation intensity (adjusted using a photometer) with time. The thickness of the cured layer was measured using a micrometer (High-Accuracy 13 Digimatic<sup>®</sup> Digital Micrometer). Afterwards, the necessary CerAM VPP process parameters—coating speed and layer exposure energy—were directly derived from the results.

### 2.4. CerAM VPP of Test Samples

With the derived parameters, first test samples of the developed AlN suspension (solid content 46 vol%) were manufactured using the CeraFab 8500 printing device (Lithoz GmbH, Vienna, Austria). Within the process, a layer of the particle-filled suspension is applied via vat rotation in combination with a static wiper blade. The bottom of the vat is transparent so the light source can locally expose the suspension from below. Using a dedicated optical system, the projected image is generated via a digital micromirror device (DMD) at a high resolution (2560 × 1600 pixels) with a pixel size of 40 μm in the x-y-plane to get a minimum material wall thickness of about 100 μm for sintered components.

At first, smaller bars and disc-shaped samples were shaped. The bars (12 × 5 × 5 mm) were manufactured in xy- and z-orientations to determine the sinter shrinkage, which is necessary to calculate the shrinkage compensation in all three dimensions. Derived from that, a printing oversize in all dimensions was considered to achieve sintered disc-shaped parts with a diameter of 12.5 mm and a thickness of 2 mm. In a third approach, a square substrate with integrated complex cooling channels was manufactured as a demonstrator. Directly after shaping the green samples, the suspension remaining on the component's surface was removed as much as possible with a specific cleaning solution (Lithasol30, Lithoz) in combination with pressured air coming from a nozzle. The next step in the

process chain was the characterization of the cleaned green bodies, including visual or microscopic sample inspection as well as size and weight measurements.

After cleaning and quality control, the green components were debinded to remove the whole polymer network and all organic compounds by heating them up to 600 °C in a nitrogen atmosphere using slow heating rates (4–10 K/h) with defined residence temperatures and dwell times (various dwell times in a range of 2 to 5 h). A very conservative temperature profile was chosen for the debinding process, which lasted about 120 h. However, some carbon remained in the structure, which was completely removed in a further tempering step up to 520 °C under an air atmosphere. Sintering was performed in a special gas furnace (Gero HT, effective volume ~5 L) at 1840 °C for 4 h and 1 bar of nitrogen atmosphere (5 L/min) with heating rates of 10 K/min up to 1400 °C and 5 K/min up to 1840 °C. Afterwards, the sintered components were examined relating to various properties.

### 2.5. Characterization of Test Samples

The shrinkage during sintering for the calculation of oversize printing was determined by measuring the dimensions of the shaped green body and of the sintered components using a caliper, and the surfaces were randomly checked for quality using an optical microscope. Afterwards, the density of the sintered discs was determined according to Archimedes' principle and converted into the relative density as a ratio to the theoretical density ( $\rho_{Th.D.} = 3.35 \text{ g/cm}^3$ ) given by the material supplier.

A further essential characteristic of the achieved material quality is the thermal conductivity, which can be determined by measuring the thermal diffusivity according to (ASTM E-1461). Using the laser-flash method, the thermal diffusivity was measured on the sintered discs (diameter: 12.5 mm, thickness: 2 mm) at room temperature. Therefore, the laser-flasher LFA427 (NETZSCH-Gerätebau GmbH, Selb, Germany), with a Nd-YAG-Laser in a wavelength of 1064 nm and a measuring range of 0.01 to 1000 mm<sup>2</sup>/s, was used. Due to transparency of the sintered AlN samples, a thin graphite layer was vapor-deposited onto the surface of the samples before measurement. The heat capacity of  $738 \pm 20 \text{ J/(kg}\cdot\text{K)}$  [42] for the AlN was used to calculate the thermal conductivity in combination with the measured density of each sample. Furthermore, the microstructure of the AlN was investigated via FESEM (SE detector; NVision ZEISS, Carl Zeiss AG, Oberkochen, Germany) of a polished cross-sectional area of the thermal conductivity disc specimen.

## 3. Results and Discussion

### 3.1. Properties of the AlN Raw Material

At the beginning of the study, the AlN raw material was investigated. The PSD was measured and can be seen in the following Figure 1 by plotting the cumulative ( $Q_3(x)$ ) and density ( $q_3(x)$ ) distributions.

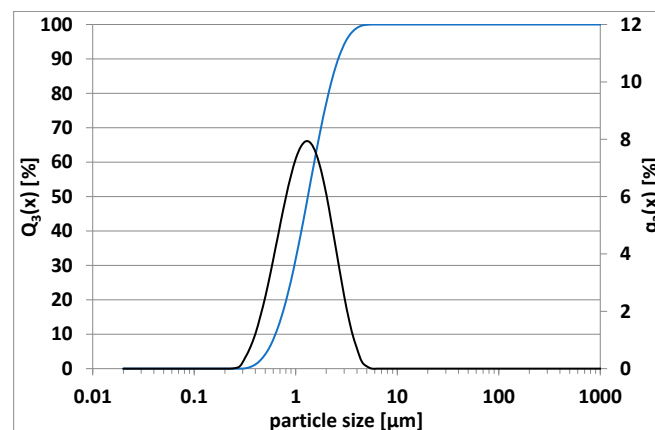


Figure 1. PSD of the AlN powder “TOYALNITE®-JCGA-BLY5”; cumulative  $Q_3(x)$  and density  $q_3(x)$ .

The result of the powder analysis shows a monomodal PSD with an average particle diameter of  $d_{50} = 1.31 \mu\text{m}$  and largest particle diameter of  $d_{100} = 4 \mu\text{m}$ . In terms of particle size, the AlN powder is thus within the required range for use in the described DLP-based CerAM VPP process and within a component layer thickness of  $25 \mu\text{m}$ . The measurement of the BET surface resulted in a value of  $3.66 \text{ m}^2/\text{g}$ , not too high and in expectation of a rather low viscosity, which should be well adjustable using the right dispersants as well as surface additives.

Decisive for the quality of a shaped component are two essential properties of the used photosensitive suspension—on one hand, the flow behavior, preferably determined by the shear rate-dependent viscosity, and on the other hand, the light-induced polymerization of the suspension dependent upon its formulation as well as the applied exposure energy. Both parameters were investigated using various methods (results presented in Sections 3.2 and 3.3) to derive a suitable CerAM VPP setting, which means process speeds (e.g., vat rotation) and the required exposure energy dose for layer-building.

### 3.2. Viscosity and Flow Behavior of Developed AlN Suspensions

As described in Section 2.4, the CerAM VPP process based on the Lithoz LCM technology works using a light-transparent vat filled with a photosensitive ceramic suspension, which is coated using a doctor blade to a thin layer of 100 to  $400 \mu\text{m}$ . A schematic representation of the suspension coating and vat rotation situation within the process has been previously described [35]. For instance, using an average coating thickness of approx.  $200 \mu\text{m}$  at a vat rotation speed of  $150^\circ/\text{s}$  is associated with shear rates up to  $1000 \text{ 1/s}$ . Due to that fact, the used photocurable suspension should have a viscosity that varies only slightly in this shear rate range, preferably within 2 powers of 10, to ensure a good layer coating. The viscosity of a suspension for this process should be not too low or too high. In the case of a viscosity that is too low, wettability problems will arise leading to pores within the green and sintered component; a viscosity that is too high will result in low flowability, and the coating of thin suspension layers cannot be guaranteed. Crucial for high-quality components is a homogeneous thin layer achievable through an ideal suspension viscosity. This requires good control of suspension viscosity, especially having a shear thinning behavior at low shear rates ( $1\text{--}10 \text{ 1/s}$ ) [43,44].

The developed AlN suspensions of this study are based on a low viscous tetrafunctional polyether acrylate and an aliphatic urethane di-acrylate mixed in a weight ratio of 7:3 and modified using a non-reactive plasticizing fluid. Therefore, only the dispersant and its contents were used to control the viscosity and stability of the developed AlN suspension.

In the first stage, the influence of the AlN content via constant dispersant content was investigated. The result can be seen in Figure 2 by plotting the dynamic viscosity dependent upon the shear rate in a solid content range of 10 to 44 vol%.

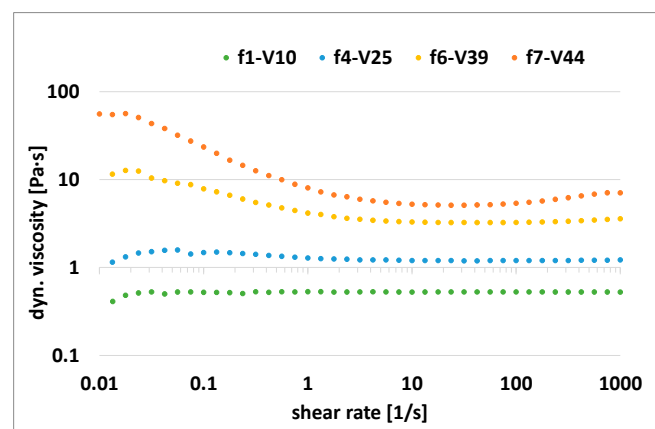


**Figure 2.** Dynamic viscosity dependent upon shear rate for AlN suspensions with varying solid content (10, 25, 39 and 44 vol%).

The result shows a Newtonian behavior in a low viscosity level for the suspensions with a low solid content up to 25 vol%. The risk of instability is naturally high here because, without an increase in viscosity at rest, the particles tend to sink down. As expected, increasing the solid content to 39 and 44 vol% resulted in a change to shear thinning behavior and a higher viscosity level, which was up to 80 Pa·s at low shear rates for a suspension of 44 vol%.

Increasing the solid content up to 48 vol% was the goal in the second stage to achieve a higher green density, which in the end should allow a higher density after sintering. Avoiding a significant increase in viscosity, the dispersant (FD) content was increased at the same time (f8–f10). The result is presented in the following graph, Figure 3.

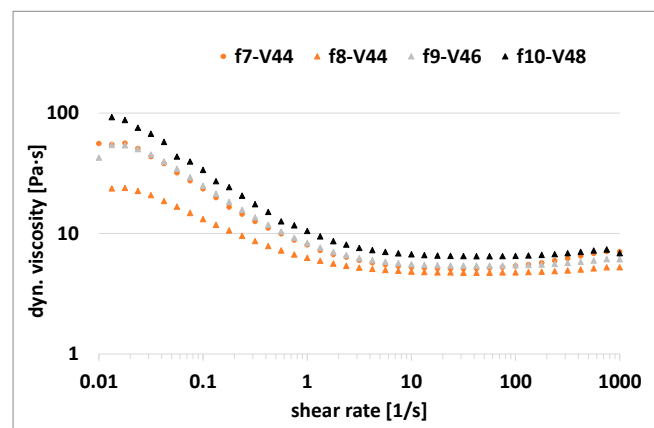


**Figure 3.** Dynamic viscosity to shear rate; AlN content of 44 (f7) and 44 to 48 vol% with increased dispersant content (f8–f10).

By increasing the FD dispersant content from 1.3 (f7) to 1.5 (f8) wt% for a suspension with 44 vol% AlN, a general decrease in viscosity was observed, especially at low shear rates (0.01 Pa·s) with 70 Pa·s to 20 Pa·s. Due to that, it was also expected to achieve low viscosity after increasing the solid contents to 46 and 48 vol%, which was confirmed by the results. The viscosity increased again with the solid content, but remained at a low level, for 46 vol% below 80 Pa·s (0.01 1/s) and nearly 100 Pa·s (0.01 1/s) for 48 vol%.

In the third stage of development, it was investigated whether the viscosity could be further decreased at low shear rates. Therefore, an alternative dispersant (AD) was used at first (f11). Afterwards, suspensions with both dispersants were prepared, with the approach to use FD to modify the powder surface and AD as a coupling agent (f12, f14). Three different proportions were investigated, as described in Section 2.2. The influence on the viscosity is shown in Figure 4 by the flow curves.

Using the alternative dispersant, the viscosity and flow behavior significantly changed to values below 10 Pa·s at shear rates of 0.01 to 80 1/s. With shear rates above 80 1/s, an unfavorable shear thickening was observed followed by a further decrease in viscosity. The change in viscosity over the shear rate range is unfavorable and should be avoided for a homogenous suspension coating in the vat within the printing process. In previous studies, it was observed that a dispersant system can help to control this behavior. Due to that, three different combinations of FD and AD were investigated. By decreasing FD to 1 wt% and using 0.5 wt% AD, the viscosity at low shear rates was reduced by 20% (f12). At the same time, the viscosity above a shear rate of 50 1/s slightly increased.

A mutual change of FD and AD content (f13) reduced the viscosity by 50% compared to f12, but a shear thickening effect was observed with a further increase in viscosity above a shear rate of 50 1/s. It was assumed that the modification of the powder surface via FD was no longer sufficient. By adjusting the FD content back to 1 wt% combined with 1 wt% of AD, the viscosity of f14 increased again, comparable to f10. In summary, an adjustment

of the viscosity is possible to a limited extent when using a system of both dispersants, with f13 as the best of the investigated combinations.

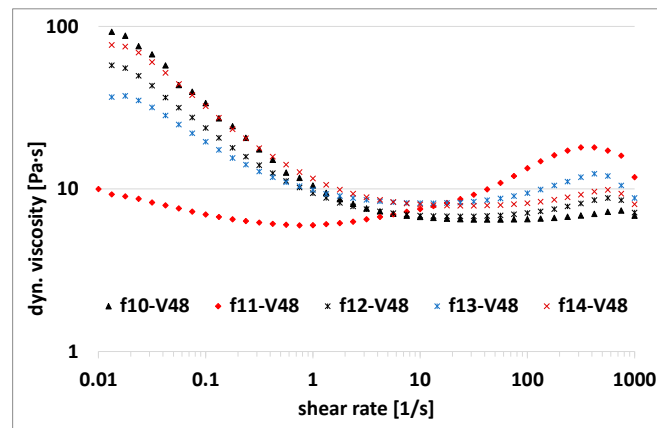


**Figure 4.** Dynamic viscosity to shear rate; AlN with 48 vol%; comparison of FD (f10) and AD (f11); dispersant system by combination of FD and AD (f12–f14).

### 3.3. Curing Behaviour of the AlN Suspensions

Besides viscosity, the most important factor for lithography-based AM technologies is the curing behavior of the photoreactive material. Especially for ceramic processing, good mechanical properties and dimensional accuracy are crucially related to the curing depth, a value mainly determined by the formulation of the photoreactive suspension. Ceramic particles within a photoreactive system act as interference centers and make photo polymerization more challenging. The photocuring light is multiple-scattered by the surfaces of the ceramic particles instead of being led into the depth during exposure, which leads to a decrease in cure depth. Jacobs et al. described the basics here 30 years ago by modelling the cure depth ( $C_D$ ) using an exponential absorption approach according to the Beer–Lambert law and the manifestation of the basic “working curve” equation of stereolithography (1), a straight-line relationship through a semi-logarithmic plot of  $C_D$  vs.  $\ln E$  [45]:

$$C_D = D_P \cdot \ln\left(\frac{E}{E_C}\right) \quad (1)$$

The penetration depth is described by  $D_P$ ,  $E$  is the energy of the light source and  $E_C$  the critical energy for the initiation of polymerization. If light hits a surface, some of the energy is absorbed and some is scattered. Ceramic particles are many submicron disturbances in a suspension, often with a large surface area, which influence and attenuate the transmission of light energy through absorption and scattering. In consequence, the energy per volume available to the photo initiator to initiate polymerization decreases with increasing layer depth [45–47].

Excessive scattering can lead to partial overexposure effects during curing, resulting in a loss of process resolution. Controlling the curing behavior is essential to achieve components of high precision. A good empirical range in which the cure depth should be controlled to avoid delamination is given with 10–35% more curing for the thickness of one layer [43].

A suitable suspension composition with useable exposure parameters was determined by investigating the relationship between cure depth and suspension formulation, especially AlN content as a function of exposure energy. Figure 5 shows a semi-logarithmic plot of the cure depth dependent upon curing energy for suspensions of different AlN contents.

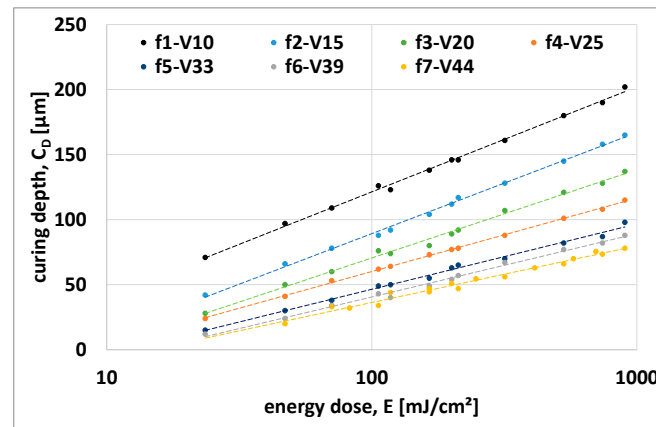


Figure 5. Curing depth via energy dose for various solid loadings.

As expected, the cure depth decreases significantly with increasing solid loading. For instance, up to a 1000 mJ/cm<sup>2</sup> energy dose for a 10 vol% AlN loading, the cure depth ranged between 75 and 200  $\mu\text{m}$ , and in contrast for a 44 vol% AlN content, the cure depth decreased to a range of 30 to 80  $\mu\text{m}$ . The penetration depth ( $D_p$ ) and the critical energy ( $E_c$ ) can be determined based on the measured values. By plotting them against the solids loading ( $\varphi$ ) (Figure 6), the dependence can be shown.

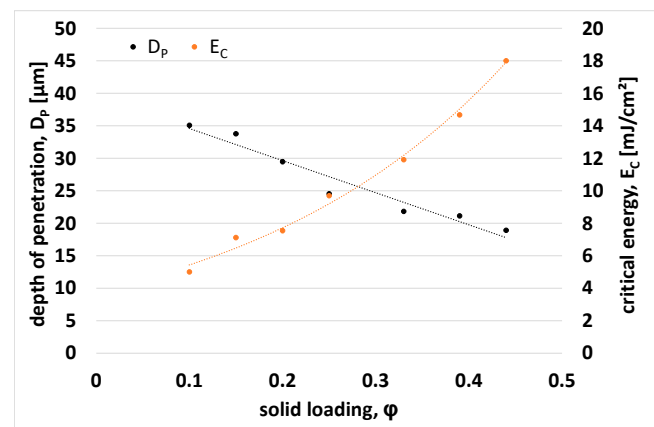


Figure 6.  $D_p$  and  $E_c$  derived from experimental data.

In agreement with Griffith et al. [48], the penetration depth is inversely proportional to solid loading and decreases linearly. The critical energy dose, on the other hand, follows an exponential function and, in contrast to the penetration depth, increases with the solid content.

In the fourth stage of development, the photosensitivity was tuned by adjusting initiator content and measuring the cure depths dependent upon exposure energy (Figure 7).

Known from a previous study [35], the initiator content influences the curing depth significantly by influencing the penetration depth and the critical energy dose. The achieved cure depth for a solid content of 44 vol% was slightly too low, with 80  $\mu\text{m}$  at a 900 mJ/cm<sup>2</sup> energy dose, as too much overexposure was detected here the same time. An increase in cure depth was necessary to achieve a better layer-by-layer connection during the shaping process without overexposure. By reducing the initiator content of I1 to  $c = 0.009$  mol/L and I2 to  $c = 0.032$  mol/L (other concentrations were also investigated but are not shown), a significant increase in cure depth with a factor of 1.25 to 2.00 dependent upon energy dose was observed. For example, the cure depth at 100 mJ/cm<sup>2</sup> increased by a value of 24  $\mu\text{m}$  from 35  $\mu\text{m}$  to 59  $\mu\text{m}$ . A comparable phenomenon was observed in a previous study [35]. By increasing the initiator content, at first  $D_p$  increased and  $E_c$  decreased, but

there is an inflection point (IP) for the initiator concentration, and afterwards  $D_P$  begins to decrease. Since  $D_P$  and  $E_C$  decrease after reaching IP,  $C_D$  also decreases, but overexposure will increase due to lower energy doses needed for polymerization initiation. In this study it is suspected that the first initiator content was too high, and the value was behind the IP. Due to the reduction of the initiator content in the fourth stage,  $D_P$  as well as  $E_C$  increased, but in total  $C_D$  increased. It is not clear if the IP was reached or not, but it will be clarified in future investigations of various initiator contents.

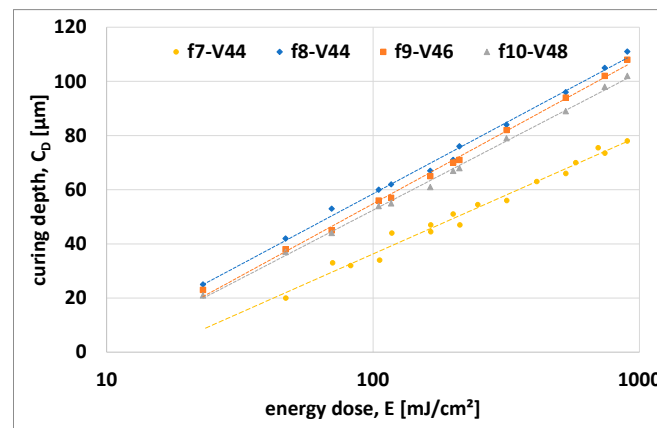


**Figure 7.**  $C_D$  after adjustment of initiator content from f7 to f8; f9 and f10, as f8.

Suspensions with a solid content of 46 and 48 vol% show a similar behavior, with a small decrease in cure depth at increasing solid contents. Based on this result, a suspension with a solid content of 46 vol%, a dispersant content such as f12, and an initiator content following the results of the fourth stage were chosen for all test samples.

### 3.4. CerAMufacturing of Test Components via CerAM VPP

At first, tests bars of 12 mm length (cross section  $5 \times 5 \text{ mm}^2$ ) and disc-like samples including shrinkage compensation (green body size: diameter  $d = 16 \text{ mm}$ , height  $h = 2.76 \text{ mm}$ ) were manufactured (Figure 8), with a building layer thickness of  $25 \mu\text{m}$  and an energy dose of  $160 \text{ mJ}/\text{cm}^2$ .



**Figure 8.** AlN-sample-discs (two views) based on suspension with 46 vol% solid content, green state.

CerAMufacturing of these green discs was successfully achieved using the derived parameters. After cleaning the components with a cleaning solution in combination with pressured air, no defects were detected through visual inspection. Afterwards, substrates with inner cooling channels were manufactured (Figure 9). Due to a smaller cross-sectional area, a larger energy dose of  $200 \text{ mJ}/\text{cm}^2$  was used for layer exposure to ensure that each layer would be adequately connected to the green body.

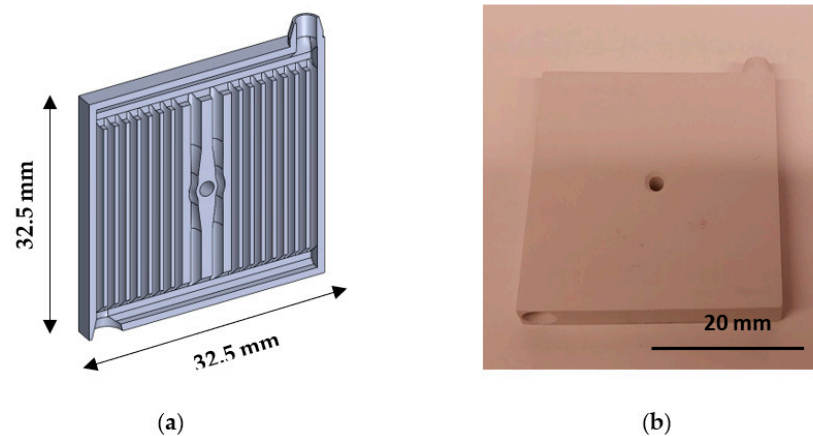


**Figure 9.** CAD substrate with integrated complex fluid channels: (a) sectional view of the CAD-design; (b) shaped component in the green state.

All green samples were cleaned, measured in all dimensions via caliper and then debinded as well as sintered followed the description of Section 2.4. The sintered components—discs and a complex substrate—are shown in Figure 10.

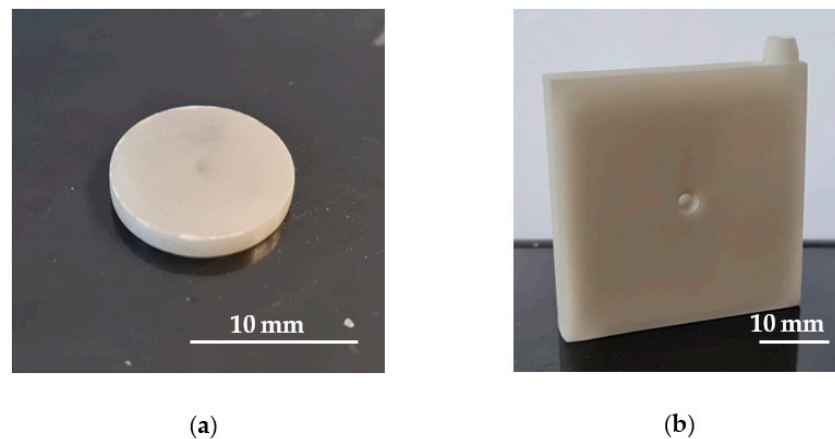


**Figure 10.** Sintered AlN parts made via CerAM VPP: (a) disc structure for TLF measurement; (b) complex substrate with inner cooling channels.

The visual inspection of all sintered samples revealed no obvious defects or cracks, which is a satisfactory result for the development state. The complex substrate with inner cooling channels was also apparently free of defects. Simple fluoroscopy with a lamp was used to screen for defects, but here also no defects became visible (Figure 11). Additionally, crack infiltration tests (Figure 11) via color solution (ARDROX-9VF2, BASF) and CT scans were taken to test the results, but they also did not show any defects as a great result.

### 3.5. Properties of Sintered AlN Components

After sintering, the density of 10 samples (discs) was measured via Archimedes' method, resulting in an average value density of  $\rho = 3.33 \pm 0.008 \text{ g/cm}^3$  ( $\rho_{\text{rel.D.}} = 99.7 \pm 0.33\%$ ) for AlN discs. With the same 10 samples, the thermal diffusivity was measured via LFA. Both results, the density and the thermal diffusivity, are presented in Figure 12.

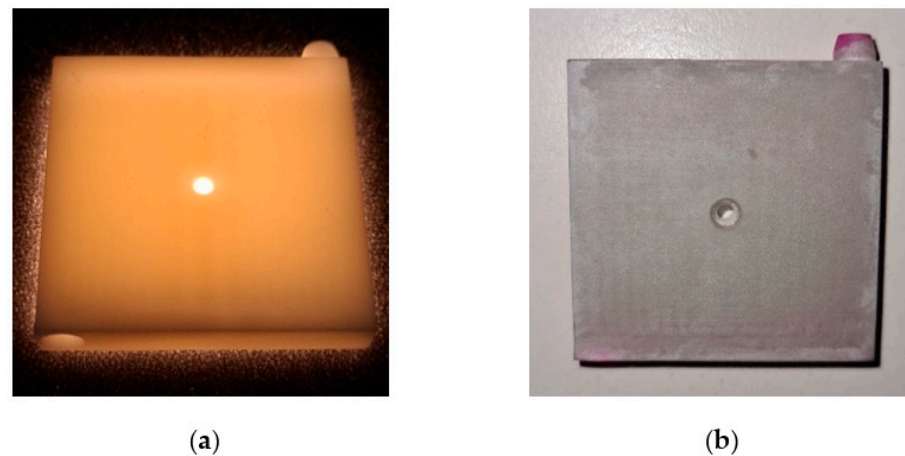


**Figure 11.** (a) Visual inspection of a complex substrate with inner cooling channels via lamp fluorescence; (b) crack infiltration test via color solution (ARDROX-9VF2).

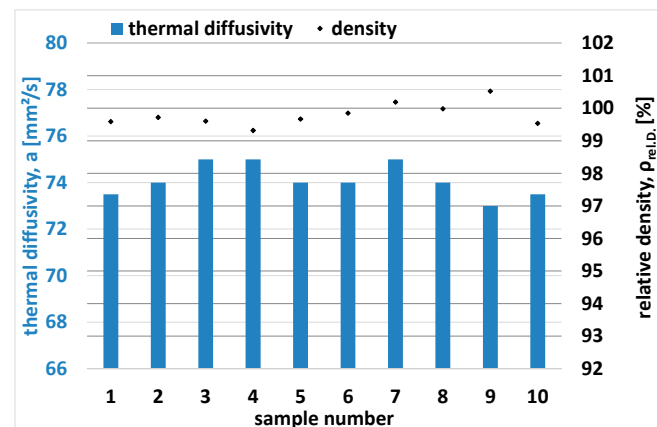


**Figure 12.** Archimedeian density (black dots) as relative density and thermal diffusivity (blue bars) measured via laser-flasher method.

Based on these results, the thermal conductivity ( $\lambda$ ) was estimated according to Equation (2):

$$\lambda = a \cdot \rho \cdot c_p \quad (2)$$

The thermal diffusivity is represented by “ $a$ ” in a product with the individual density  $\rho$  and the specific heat capacity  $c_p$  (room temperature). The calculated thermal conductivities of 10 samples are presented in Figure 13.

The measured thermal diffusivity reached very homogeneous values, in a range of 73 to 75 mm<sup>2</sup>/s, and therefore, in combination with the measured density, led to thermal conductivities with an average value of  $182 \pm 1.5$  W/(m·K), a very good result for AlN corresponding to the powder supplier’s specifications for pressed components.

Supporting the results of the achieved densities as well as the thermal conductivities, the microstructure of a polished cross-section of a sintered disc was analyzed via FESEM (Figure 14).

The AlN components were heated through a standard program using a constant heating rate of 5 K/min up to 1840 °C with 4 h dwell time. In general, the images show a homogeneous AlN microstructure. The secondary phase (yttria) can be distinguished from AlN by its brighter contrast (white grains). Clusters of them could not be found. All microstructures confirmed high densification as evidenced by well-developed polyhedral AlN grains. In the direction of the sample surface, the yttria amount increases and forms a kind of boundary layer in which the yttria content seem to be higher compared to the main

part of the structure. During sintering, the yttria tends to excrete on the surface. However, this is intentional to achieve a high thermal conductivity over the entire structure. In general, the microstructure of the sintered AlN shows a good quality, comparable standard AlN, especially created through conventional shaping. A layered structure could not be identified.

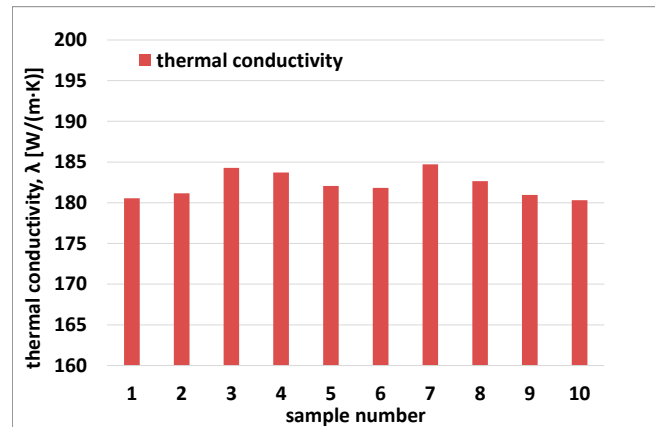


Figure 13. Calculated thermal conductivity  $\lambda$  of 10 samples.

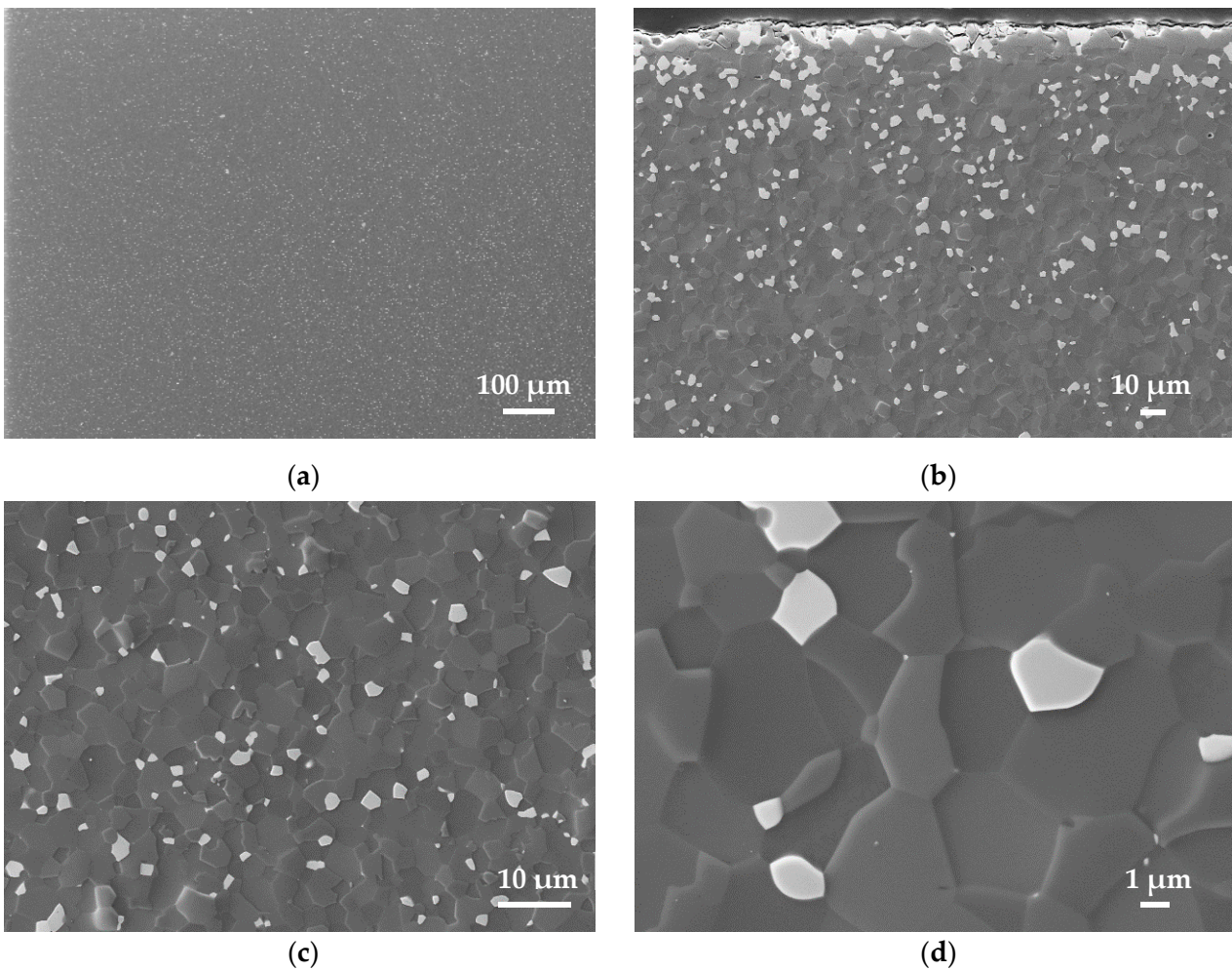


Figure 14. FESEM micrographs (SE detector) of additively manufactured AlN samples (polished cross-sections) in various magnifications, sintered at 1840 °C with 4 h dwell time: (a) magnification 35 $\times$ ; (b) magnification 500 $\times$ ; (c) magnification 1000 $\times$ ; (d) magnification 5000 $\times$ .

#### 4. Conclusions

Meeting the constantly increasing demands on substrate materials and heat sinks resulting from the permanent increase in power density, and thus also in heat generation in electronic components, new types of components made of high-performance materials with highly complex geometries are required. AlN is predestined as such a material because it has a unique combination of high thermal and very low electrical conductivity.

In this work, AlN has been successfully qualified as an AM technology. Based on a commercial powder, the suspension and process development for CerAM VPP was carried out, which is a DLP-based vat photo polymerization technology, to realize sintered components with excellent thermal properties and comparable achieved values of conventional shaping methods (approx. 180 W/(m·K)).

Photoreactive suspensions were developed, and the influence of the AlN content up to 48 vol% on viscosity and photosensitivity was investigated. Afterwards, the flow and curing behavior were slightly optimized using a dispersant system and an adjustment of the initiator content.

Based on the results of the suspension characterization, CerAM VPP process parameters for the CerAMufacturing of test components were derived. Test components with different geometries were CerAMufactured, debinded and sintered.

The properties of the components were characterized along the entire process chain. The achieved densities of 3.33 g/cm<sup>3</sup> ( $\rho_{\text{rel.D.}} = 99.7\%$ ) and thermal conductivities larger than 180 W/(m·K) are excellent and comparable to state-of-the-art for conventionally manufactured components. The microstructure is homogeneous and of good quality, confirming the measured density and thermal conductivity.

A substrate with a complex inner design of cooling channels was used to demonstrate the successful CerAMufacturing of complex AlN components. Further work and publication will address AlN components with application-specific designs as well as the mechanical characterization of AlN components.

**Author Contributions:** Conceptualization, E.S.-F.; methodology, E.S.-F. and U.S.; formal analysis, E.S.-F, U.S. and A.M.; investigation, E.S.-F.; resources, E.S.-F, U.S. and A.M.; data curation, E.S.-F, U.S. and A.M.; writing—original draft preparation, E.S.-F.; writing—review and editing, E.S.-F. and U.S.; visualization, E.S.-F.; supervision, U.S. and A.M. All authors have read and agreed to the published version of the manuscript.

**Funding:** This research received no external funding.

**Institutional Review Board Statement:** Not applicable.

**Informed Consent Statement:** Not applicable.

**Data Availability Statement:** The data are not publicly available due to data confidentiality resulting from the requirements of the accreditation.

**Acknowledgments:** Many thanks go to Jan Räthel, who provided advice and support regarding AlN, and special thanks go to Mathias Herrmann (among other things, a specialist in microstructure analysis and AlN materials) for his support in the analysis of our sintered microstructures and its evaluation.

**Conflicts of Interest:** The authors declare no conflict of interest.

#### References

1. Material Properties of Our Fully Ceramic Heating Elements. Available online: <https://www.bachrc.de/material.html?language=en> (accessed on 21 December 2022).
2. Innovative Thermal Management with Ceramic Heat-Sink. Available online: <https://www.ceramtec-industrial.com/en/products-applications/heat-sinks> (accessed on 21 December 2022).
3. Miyashiro, F.; Iwase, N.; Tsuge, A.; Ueno, F.; Nakahashi, M.; Takahashi, T. High thermal conductivity aluminum nitride ceramic substrates and packages. *IEEE Trans. Components, Hybrids Manuf. Technol.* **1990**, *13*, 313–319. [CrossRef]
4. Baik, Y.; Drew, R.A.L. Aluminum nitride: Processing and applications. *Key Eng. Mater.* **1996**, *553*, 122–124.

5. CeramCool® Principle and Function. Available online: <https://www.ceramtec-industrial.com/en/products-applications/heat-sinks/ceramcool-principle-function> (accessed on 21 December 2022).
6. Variety of Shapes and Options for Virtually Every Cooling Capacity. Available online: <https://www.ceramtec-industrial.com/en/products-applications/heat-sinks/ceramcool-design-data> (accessed on 21 December 2022).
7. Aluminium Nitride AlN. Available online: <https://www.final-materials.com/gb/39-aluminium-nitride-aln> (accessed on 21 December 2022).
8. Aluminum Nitride (AlN) Components. Available online: <https://www.maruwa-g.com/e/products/ceramic/000614.html> (accessed on 21 December 2022).
9. Aluminum Nitride (AlN). Available online: <https://www.ceramtec-industrial.com/en/materials/aluminum-nitride> (accessed on 21 December 2022).
10. Watari, K.; Ishizaki, K.; Fujikawa, T. Thermal conduction mechanism of aluminium nitride ceramics. *J. Mater. Sci.* **1992**, *27*, 2627–2630. [[CrossRef](#)]
11. Potter, G.E.; Knudsen, A.K.; Tou, J.C.; Choudhury, A. Measurement of the oxygen and impurity distribution in polycrystalline aluminum nitride with secondary ion mass spectrometry. *J. Am. Ceram. Soc.* **1992**, *75*, 3215–3224. [[CrossRef](#)]
12. Slack, G.A.; Tanzilli, R.A.; Pohl, R.O.; Vandersande, J.W. The intrinsic thermal conductivity of AlN. *J. Phys. Chem. Solid.* **1987**, *48*, 641–647. [[CrossRef](#)]
13. Troczynski, T.B.; Nicholson, P.S. Effect of additives on the pressureless sintering of aluminum nitride between 1500° and 1800 °C. *J. Am. Ceram. Soc.* **1989**, *72*, 1488–1491. [[CrossRef](#)]
14. Cao, Y.; Xu, H.; Zhan, J.; Zhang, H.; Song, C.; Tang, W. Microstructure, Growth Kinetics and Formation Mechanism of Oxide Layers on AlN Ceramic Substrates. *J. Ceram. Sci. Technol.* **2018**, *9*, 263–270.
15. Lee, R.R. Development of high thermal conductivity aluminum nitride ceramic. *J. Am. Ceram. Soc.* **1991**, *74*, 2242–2249. [[CrossRef](#)]
16. Fu, R.; Chen, K.; Agathopoulos, S.; Ferro, M.C.; Tulyaganov, D.U.; Ferreira, J.M.F. Migration of liquid phase in low temperature sintering of AlN. *J. Mater. Sci.* **2005**, *40*, 2425–2429. [[CrossRef](#)]
17. Watari, K.; Tsuzuki, A.; Torii, Y. Effect of rare-earth oxide addition on the thermal conductivity of sintered aluminium nitride. *J. Mater. Sci. Lett.* **1992**, *11*, 1508–1510. [[CrossRef](#)]
18. Virkar, A.V.; Jackson, T.B.; Cutler, R.A. Thermodynamic and kinetic effects of oxygen removal on the thermal conductivity of aluminum nitride. *J. Am. Ceram. Soc.* **1989**, *72*, 2031–2042. [[CrossRef](#)]
19. Watari, K. High thermal conductivity non-oxide ceramics. *J. Ceram. Soc. Jpn.* **2001**, *109*, S7–S16. [[CrossRef](#)]
20. Beyer, S.; Brunner, D.; Gottschalk, T.; Jaenicke-Rößler, K.; Leitner, G.; Raether, F.; Ruska, J.; Thimm, A. Kosten- und Qualitätsoptimierung bei der Sinterung von AlN-Keramik. *Beitrag Zur Werkstoffwoche. Mater.* **1998**.
21. Mussler, B.; Brunner, D. Aluminiumnitridkeramik. *Tech. Keram. Werkst. (DKG)* **2001**, *66*, 1–33.
22. Hirano, M.; Kato, K.; Isobe, T.; Hirano, T. Sintering and characterization of fully dense aluminium nitride ceramics. *J. Mater. Sci.* **1993**, *28*, 4725–4730. [[CrossRef](#)]
23. Liu, S.; Ye, F.; Liu, L.; Liu, Q.; Li, J. Preparation of aluminum nitride ceramics by aqueous tape casting. *Mater. Manuf. Process.* **2015**, *30*, 605–610. [[CrossRef](#)]
24. Luo, X.; Zhang JLi, B.; Zhuang WLi, H. High thermal conductivity aluminum nitride substrates prepared by aqueous tape casting. *J. Am. Ceram. Soc.* **2006**, *89*, 836–841. [[CrossRef](#)]
25. Aluminium Nitride Product/ALN Heat Sink. Available online: <https://top-seiko.com/works/aluminum-nitride14/> (accessed on 21 December 2022).
26. Travitzky, N.; Bonet, A.; Dermeik, B.; Fey, T.; Filbert-Demut, I.; Schlier, L.; Schlordt, T.; Greil, P. Additive Manufacturing of Ceramic-Based Materials. *Adv. Eng. Mater.* **2014**, *16*, 729–754. [[CrossRef](#)]
27. Chen, Z.; Sun, X.; Shang, Y.; Xiong, K.; Xu, Z.; Guo, R.; Cai, S.; Zheng, C. Dense ceramics with complex shape fabricated by 3D printing: A review. *J. Adv. Ceram.* **2021**, *10*, 195–218. [[CrossRef](#)]
28. Belmonte, M.; Lopez-Navarrete, G.; Osendi, M.I.; Miranzo, P. Heat dissipation in 3D printed cellular aluminum nitride structures. *J. Eur. Ceram. Soc.* **2021**, *41*, 2407–2414. [[CrossRef](#)]
29. Aguilar, A.C.; Diaz-Moreno, C.A.; Price, A.D.; Goutam, R.K.; Botez, C.E.; Lin, Y.; Wicker, R.B.; Li, C. Non-destructive optical second harmonic generation imaging of 3D printed aluminum nitride ceramics. *Ceram. Int.* **2019**, *45*, 18871–18875. [[CrossRef](#)]
30. Diaz-Moreno, C.A.; Rodarte, C.; Ambriz, S.; Bermudez, D.; Roberson, D.; Terrazas CEspalin, D.; Ferguson, R.; Shafirovich, E.; Lin, Y. Binder jetting of high temperature and thermally conductive (aluminum nitride) ceramic. In Proceedings of the 29th Annual International Solid Freeform Fabrication Symposium, Austin, TX, USA, 13–15 August 2018; pp. 143–159.
31. Halloran, J.W. Ceramic Stereolithography: Additive Manufacturing for Ceramics by Photopolymerization. *Annu. Rev. Mater. Res.* **2016**, *46*, 19–40. [[CrossRef](#)]
32. Zakeri, S.; Vippola, M.; Levänen, E. A comprehensive review of the photopolymerization of ceramic resins used in stereolithography. *Addit. Manuf.* **2020**, *35*, 101177. [[CrossRef](#)]
33. Rasaki, S.A.; Xiong, D.; Xiong, S.; Su, F.; Idrees, M.; Chen, Z. Photopolymerization-based additive manufacturing of ceramics: A systematic review. *J. Adv. Ceram.* **2021**, *10*, 442–471. [[CrossRef](#)]
34. Altun, A.A.; Prochaska, T.; Konegger, T.; Schwentenwein, M. Dense, Strong, and Precise Silicon Nitride-Based Ceramic Parts by Lithography-Based Ceramic Manufacturing. *Appl. Sci.* **2020**, *10*, 996. [[CrossRef](#)]

35. Schwarzer-Fischer, E.; Zschippang, E.; Kunz, W.; Koplin, C.; Löw, Y.M.; Scheithauer UMichaelis, A. CerAMufacturing of silicon nitride by using lithography-based ceramic vat photopolymerization (CerAM VPP). *J. Europ. Ceram. Soc.* **2022**, *43*, 321–331. [[CrossRef](#)]
36. Ding, G.; He, R.; Zhang, K.; Xie, C.; Wang, M.; Yang, Y.; Fang, D. Stereolithography-based additive manufacturing of gray-colored SiC ceramic green body. *J. Am. Ceram. Soc.* **2019**, *102*, 7198–7209. [[CrossRef](#)]
37. Rauchenecker, J.; Rabitsch, J.; Schwentenwein, M.; Konegger, T. Additive manufacturing of aluminum nitride ceramics with high thermal conductivity via digital light processing. *Open Ceram.* **2022**, *9*, 100215. [[CrossRef](#)]
38. Ozóg, P.; Rutkowski, P.; Kata, D.; Graule, T. Ultraviolet lithography-based ceramic manufacturing (UV-LCM) of the aluminum nitride (AlN)-Based photocurable dispersions. *Materials* **2020**, *13*, 4219. [[CrossRef](#)]
39. Lin, L.; Wu, H.; Xu, Y.; Lin, K.; Zou, W.; Wu, S. Fabrication of dense aluminum nitride ceramics via digital light processing-based stereolithography. *Mater. Chem. Phys.* **2020**, *249*, 122969. [[CrossRef](#)]
40. Duan, W.; Li, S.; Wang, G.; Dou, R.; Wang, L.; Zhang, Y.; Li, H.; Tan, H. Thermal conductivities and mechanical properties of AlN ceramics fabricated by three dimensional printing. *J. Eur. Ceram. Soc.* **2020**, *40*, 3535–3540. [[CrossRef](#)]
41. Johansson, E.; Lidström, O.; Johansson, J.; Lyckfeldt, O.; Adolfsson, E. Influence of Resin Composition on the Defect Formation in Alumina Manufactured by Stereolithography. *Materials* **2017**, *10*, 138. [[CrossRef](#)] [[PubMed](#)]
42. ICT-ALN. Available online: <https://www.ict-suedwerk.de/de/products/Cer-T/-Thermally-Conductive-Technical-Ceramics-ICT-ALN,168> (accessed on 21 December 2022).
43. Halloran, J.W.; Tomeckova, V.; Gentry, S.; Das, S.; Cilino, P.; Yuan, D.; Guo, R.; Rudraraju, A.; Shao, P.; Wu, T.; et al. Photopolymerization of powder suspensions for shaping ceramics. *J. Europ. Ceram. Soc.* **2011**, *31*, 2613–2619. [[CrossRef](#)]
44. Schwarzer, E.; Holtzhausen, S.; Scheithauer, U.; Ortmann, C.; Oberbach, T.; Moritz, T.; Michaelis, A. Process development for additive manufacturing of functionally graded alumina toughened zirconia components intended for medical implant application. *J. Europ. Ceram. Soc.* **2019**, *39*, 522–530. [[CrossRef](#)]
45. Jacobs, P.F. *Fundamentals of Stereolithography*; 3D Systems, Inc.: Valencia, CA, USA, 1992; pp. 196–211.
46. Griffith, M.L.; Halloran, J.W. Freeform Fabrication of Ceramics via Stereolithography. *J. Am. Ceram. Soc.* **1996**, *79*, 2601–2608. [[CrossRef](#)]
47. Zimbeck, W. Stereolithography of Ceramics and Metals. In *IS&T's 50th Annual Conference*; The Society for Imaging Science and Technology: Cambridge, MA, USA, 1997; Volume 50, pp. 649–655.
48. Griffith, M.L.; Halloran, J.W. Scattering of ultraviolet radiation in turbid suspensions. *Appl. Phys.* **1997**, *81*, 2538–2546. [[CrossRef](#)]

**Disclaimer/Publisher's Note:** The statements, opinions and data contained in all publications are solely those of the individual author(s) and contributor(s) and not of MDPI and/or the editor(s). MDPI and/or the editor(s) disclaim responsibility for any injury to people or property resulting from any ideas, methods, instructions or products referred to in the content.